Lattice-Boltzmann algorithm for simulating thermal two-phase flow

Bruce J. Palmer and David R. Rector
Environmental and Molecular Sciences Laboratory, Box 999, Pacific Northwest National Laboratory, Richland, Washington 99352*
(Received 20 August 1999)

An algorithm is described for incorporating thermal effects into lattice-Boltzmann simulations of two-phase flow. This algorithm is a combination of a two-distribution model for simulating single-phase thermal flow recently proposed by the authors and the thermodynamically-based model for isothermal two-phase flow of Swift *et al.* [Phys. Rev. E **54**, 5041 (1996)]. The algorithm also corrects a problem with the original single-phase thermal flow model, which described the thermal energy flux as proportional to a gradient of the internal energy instead of being proportional to the gradient of the temperature. For ideal-gas systems, these two descriptions are equivalent but for nonideal systems there is a systematic discrepancy between the original thermal model and classical hydrodynamics. The algorithm is tested on several simple problems. These include formation of a free-standing isothermal thin liquid film, evaporation of a thin liquid film from a heated plate, evaporation of an isolated droplet, and condensation of liquid in a channel. Where possible, the simulations are compared against known analytic results.

PACS number(s): 47.55.Kf, 47.11.+j, 02.70.−c, 05.70.Fh

I. INTRODUCTION

Lattice-Boltzmann algorithms have recently begun to receive considerable attention as a possible alternative to conventional computational fluid dynamics (CFD) for simulating fluid flow. These algorithms have shown great promise for simulating flow in topologically complicated geometries, such as those encountered in porous media, and for simulating flow in multiphase systems. This is especially true for simulations of multiphase flow, where there are few, if any, viable alternatives using conventional CFD approaches. The standard hydrodynamic approach is to model the system as two or more distinct fluids separated by an infinitely thin mathematical boundary. The behavior of each fluid is described using a standard hydrodynamic description and the fluids are coupled to each other by appropriate boundary conditions at the interface. The boundary conditions can also be used to develop an equation of motion for the interface. The fact that the interface is itself a dynamic quantity, however, creates prodigious problems from the numerical point of view. If a conventional grid is used for each of the fluid components, then front-tracking routines are needed for appropriately adjusting the grid as the interface location changes and the CFD solvers need to be modified to reflect the time-dependence of the grid itself. The problem is further complicated if the topology of the two fluids changes. An example of this would be a drop of one fluid breaking off and penetrating into the other fluid during a mixing operation. While these processes are expected to occur in most multiphase flows of practical interest, they add enormously to the complexity of the calculation. Because of this, only a relatively small number of problems have been successfully tackled using a front-tracking approach [1].

An alternative to front tracking is to incorporate two-phase behavior directly into the equation describing the fluid. This is the approach taken in lattice-Boltzmann simulations, but it has also been employed to a limited extent in more traditional CFD contexts [2,3]. Using a single equation to model both phases has the considerable advantage of eliminating front tracking. Instead, the interface is modeled as a continuous function of the thermodynamic properties of the fluid. The interface is no longer a mathematically discrete boundary, but is broadened out into a continuous variation in fluid properties that typically extends over several grid spacings. This implies that the grid being used for the simulation must be fine enough to resolve the interface, which will typically be much narrower than most other features in the problem. Furthermore, since the interface can wander around anywhere in the simulation, the grid must be relatively uniform throughout the fluid volume. This means that lattice-Boltzmann algorithms, most of which have been developed for regular grids, are not a significant disadvantage with respect to CFD algorithms, which can usually handle more general grid structures.

Several lattice Boltzmann algorithms have been developed in the last few years for simulating multiphase and multicomponent flows in isothermal systems. These include the model of Shan and Chen [4,5], which uses a nonlocal force in the algorithm to force the spontaneous formation of distinct liquid and vapor phases under appropriate conditions, and the model of Swift *et al.* [6], which incorporates a thermodynamically-based description of the two-phase system into the simulation from the start. These models have been successfully used to model a number of multiphase and/or multicomponent flow problems under isothermal conditions. However, they have not been extended to include the effects of temperature and therefore cannot be used to investigate systems where thermal transport limits the rate of phase change. This includes many important problems such as boiling, distillation, and the dynamics of phase separation. Until recently, incorporating thermal behavior into the multiphase models has been hampered by the lack of a suitable

*Pacific Northwest National Laboratory is operated for the U.S. Department of Energy by Battelle Memorial Institute under Contract No. DE-AC06-76RLO 1830.

lattice Boltzmann model for describing thermal flow, even in single-phase systems.

This paper will describe a lattice Boltzmann algorithm that is capable of modeling thermal flow in two-phase systems. The algorithm is a combination of the two-phase isothermal model of Swift *et al.* [6] and the two-distribution model for thermal flow recently proposed by the authors [7]. The two-distribution model treats the internal energy as a separate conserved scalar (similar to the density) that is modeled by its own discretized Boltzmann distribution. This approach is fairly stable and easy to implement; it can handle arbitrary values of the Prandtl number, and an arbitrary equation of state can be used. Several other algorithms based on using only a single discretized Boltzmann distribution have been limited by issues of numerical stability and the ability to only simulate one value of the Prandtl number [8,9]. These other algorithms also appear to be restricted to modeling fluids with an ideal gas equation of state. Recently, He, Chen, and Doolen developed a two-distribution model that they obtained rigorously from a BGK approximation to the Boltzmann equation [10]. However, this algorithm is also restricted to systems with ideal-gas thermodynamics. This is a major drawback when considering multiphase flow, where the equation of state must necessarily be nonideal.

The details of the thermal two-phase model are described in Sec. II. The hydrodynamic equations for the model are derived and used to determine the parameters that appear in the equilibrium distribution functions. The model not only allows the formation of multiple phases, but also fixes a problem in the original two-distribution thermal model related to the form of the thermal energy flux. Finally, the results of simulations performed on a free-standing liquid film, evaporation of a liquid film from a heated plate, evaporation of a droplet, and condensation of vapor in a channel under the influence of gravity are described.

II. THERMAL TWO-PHASE MODEL

Lattice-Boltzmann simulations are an alternative to classical fluid dynamics that attempt to model fluid flow by simulating the behavior of the one-particle distribution function [11,12]. The original Boltzmann equation describes the behavior of the one-particle distribution function, $f(\mathbf{r},\mathbf{v},t)$, where f represents the probability that a fluid particle can be found at the point $\mathbf{r}$ at time t, moving with velocity $\mathbf{v}$. If this function is known, then local values of the mass, momentum, and temperature can be found by evaluating moments of f. The other thermodynamic properties can then be found from the density and temperature through the equation of state. Instead of a continuous function f, the lattice Boltzmann distribution function is discretized so that space is divided up into a regular lattice and the velocities are represented by a finite number of displacements to neighboring lattice sites. The displacement vectors are denoted by $\Delta t\mathbf{e}_i$, where $i=1,\cdots,b$, $\mathbf{e}_i$ is the displacement velocity, Δt is the discrete timestep, and b represents the total number of displacement directions. The magnitude of the displacement velocity is $|\mathbf{e}_i|=c$ and a zero displacement vector $\mathbf{e}_0$ is included in the set to represent particles with zero velocity. Note that in this formulation c has units of velocity. The derivations described below assume that the lattices represented by the vectors $\mathbf{e}_i$ are suitably symmetric so that the tensors $\Sigma_{i=1}^{b}\mathbf{e}_i\mathbf{e}_i$ and $\Sigma_{i=1}^{b}\mathbf{e}_i\mathbf{e}_i\mathbf{e}_i\mathbf{e}_i$ are isotropic. As has been pointed out by several authors, suitably isotropic lattices are known only in two and four dimensions [13,14]. However, three-dimensional simulations can be recovered by using a four-dimensional lattice and making the system completely uniform along one of the axes.

Two sets of discretized distributions, f_i and F_i, are assigned to each site. The distribution f_i models the transport of mass and momentum and satisfies the moment relations

$$\rho=\sum_{i=0}^{b} f_i, \tag{2.1}$$

$$\rho\mathbf{u}=\sum_{i=1}^{b} \mathbf{e}_i f_i, \tag{2.2}$$

where ρ is the mass density and $\mathbf{u}$ is the macroscopic velocity of the fluid. The distribution F_i models the movement of internal energy through the system and satisfies the moment relation

$$\rho\epsilon=\sum_{i=0}^{b} F_i, \tag{2.3}$$

where ϵ is the specific energy per unit mass.

The distributions are updated at each time step by first performing a collision to obtain a new set of distributions and then displacing the f_i and F_i along the vector $\mathbf{e}_i$ to get a new set of distributions at each site. The collisions and displacement of the distributions are summarized by the equations of motion

$$f_i(\mathbf{r}+\Delta t\mathbf{e}_i,t+\Delta t)-f_i(\mathbf{r},t)=-\frac{1}{\tau_\rho}[f_i(\mathbf{r},t)-f_i^{eq}(\mathbf{r},t)], \tag{2.4}$$

$$F_i(\mathbf{r}+\Delta t\mathbf{e}_i,t+\Delta t)-F_i(\mathbf{r},t)=-\frac{1}{\tau_\epsilon}[F_i(\mathbf{r},t)-F_i^{eq}(\mathbf{r},t)], \tag{2.5}$$

where the $\mathbf{r}$ are restricted to sites on the lattice and t is the discrete time. The collision terms in the equations of motion have the familiar Bhatnagar, Gross, and Krook (BGK) form [15] and are characterized for the two distributions by the dimensionless relaxation parameters τ_ρ and τ_ϵ. Because there is no explicit coupling between the equations of motion for the f_i and F_i, the total internal energy of the system is a conserved quantity, implying that there is no viscous heating in the system. For many problems of practical importance, the contribution from viscous heating is small. Where they are non-negligible, additional enhancements to the model will be required.

To completely describe the algorithm, the equilibrium distributions f_i^{eq} and F_i^{eq} need to be specified. Following Swift *et al.* [6], the equilibrium mass-momentum distribution f_i^{eq} is chosen to have the form

$$f_i^{eq}=A+\frac{\rho D}{bc^2}e_{i\alpha}u_\alpha+\frac{\rho D(D+2)}{2bc^4}e_{i\alpha}e_{i\beta}u_\alpha u_\beta - \frac{\rho D}{2bc^2}u_\alpha u_\alpha+E_{\alpha\beta}e_{i\alpha}e_{i\beta}, \tag{2.6}$$

$$f_0^{eq}=A_0-\frac{\rho}{c^2}u_\alpha u_\alpha. \tag{2.7}$$

The spatial components are labeled by Greek indices and the Einstein convention of summing over repeated indices is used. The variable D is the dimension of the lattice and the parameters A, A_0, and the $E_{\alpha\beta}$ will be determined later. Similarly, the equilibrium energy distribution F_i^{eq} is chosen to have the form

$$F_i^{eq}=B+\frac{\rho\epsilon D}{bc^2}e_{i\alpha}u_\alpha+\frac{\rho\epsilon D(D+2)}{2bc^4}e_{i\alpha}e_{i\beta}u_\alpha u_\beta - \frac{\rho\epsilon D}{2bc^2}u_\alpha u_\alpha+G_\alpha e_{i\alpha}+H_{\alpha\beta}e_{i\alpha}e_{i\beta}, \tag{2.8}$$

$$F_0^{eq}=B_0-\frac{\rho\epsilon}{c^2}u_\alpha u_\alpha. \tag{2.9}$$

Again, the parameters B, B_0, G_α, and $H_{\alpha\beta}$ will be determined later. The extra term $G_\alpha e_{i\alpha}$ in the F_i^{eq} is new and is used to correct the form of the thermal diffusion term. It turns out that this is essential for producing a stable temperature profile through the interface. The equilibrium distributions are also required to satisfy the moment relations (2.1)–(2.3).

Once the equilibrium distributions have been specified, the lattice-Boltzmann algorithm consists of the following steps:

(i) Calculate ρ, $\mathbf{u}$, and ϵ at each site using the moment relations (2.1)–(2.3).

(ii) Based on the values of ρ and ϵ, evaluate the parameters in the equilibrium distribution functions via some as yet unspecified relations.

(iii) Evaluate f_i^{eq} and F_i^{eq} at each site and complete the collision step.

(iv) Translate the f_i and F_i.

To find expressions for the undetermined parameters in the equilibrium distributions, it is first necessary to calculate what kinds of hydrodynamic equations are generated by this algorithm. The parameters are then determined by the requirement that the hydrodynamic equations generated by the model match the equations of classical hydrodynamics.

To produce two-phase behavior, the hydrodynamic equations are modified so that the scalar hydrostatic pressure is replaced by the pressure tensor. The pressure tensor must be generalized to include off-diagonal terms that account for the nonisotropic stresses that occur when an interface is introduced into the system. Following Swift *et al.* [6], the Cahn-Hilliard form [16]

$$P_{\alpha\beta}=p\,\delta_{\alpha\beta}+\kappa(\partial_\alpha\rho)(\partial_\beta\rho), \tag{2.10}$$

$$p=p_0-\kappa\rho\partial_\alpha\partial_\alpha\rho-\frac{\kappa}{2}(\partial_\alpha\rho)(\partial_\alpha\rho) \tag{2.11}$$

is used in this work for the pressure tensor. The function $p_0=p_0(\rho,\epsilon)$ is the ordinary equilibrium pressure for a uniform system given by the equation of state and κ is a parameter controlling the surface tension.

III. DERIVATION OF THE HYDRODYNAMIC EQUATIONS

For multiphase systems the standard Chapman-Enskog multiple time-scale analysis [13] for deriving the hydrodynamic behavior is no longer useful. The problem occurs because of the expected appearance of interfaces, which create short-ranged changes in the density, internal energy, and velocity. These terms appear as higher-order terms in the Chapman-Enskog expansion where they are typically discarded. (The multiple time-scale analysis projects out the long time-scale, long-wavelength behavior of the system. The terms responsible for the interface do not show up because the interface is an inherently short-ranged phenomena.) The Chapman-Enskog analysis does provide hydrodynamic equations that describe the single-phase behavior of the model, but does not give any information about the extra terms necessary to create two coexisting phases. Instead of the Chapman-Enskog expansion, this paper will therefore use the method of successive approximations described by Swift *et al.* [6] to determine the hydrodynamic equations. A brief outline of this method is given below, most of the details are provided in the Appendix.

This analysis begins by expanding the equations of motion about $\mathbf{r}$ and t to second order in Δt. Equations that express the behavior of the unknown distributions f_i and F_i in terms of the corresponding equilibrium distributions can be obtained by recursively substituting these expansions into themselves. After truncating the expansions at second order in Δt, the following equations are obtained:

$$-\frac{1}{\Delta t\tau_\rho}(f_i-f_i^{eq})=\frac{\partial}{\partial t}f_i^{eq}+e_{i\alpha}\partial_\alpha f_i^{eq} - \Delta t\frac{\partial}{\partial t}\left(\tau_\rho-\frac{1}{2}\right)\left(\frac{\partial}{\partial t}+e_{i\alpha}\partial_\alpha\right)f_i^{eq} - \Delta t e_{i\alpha}\partial_\alpha\left(\tau_\rho-\frac{1}{2}\right)\left(\frac{\partial}{\partial t}+e_{i\beta}\partial_\beta\right)f_i^{eq}, \tag{3.1}$$

$$-\frac{1}{\Delta t\tau_\epsilon}(F_i-F_i^{eq})=\frac{\partial}{\partial t}F_i^{eq}+e_{i\alpha}\partial_\alpha F_i^{eq} - \Delta t\frac{\partial}{\partial t}\left(\tau_\epsilon-\frac{1}{2}\right)\left(\frac{\partial}{\partial t}+e_{i\alpha}\partial_\alpha\right)F_i^{eq} - \Delta t e_{i\alpha}\partial_\alpha\left(\tau_\epsilon-\frac{1}{2}\right)\left(\frac{\partial}{\partial t}+e_{i\beta}\partial_\beta\right)F_i^{eq}. \tag{3.2}$$

The moment relations can be applied to Eqs. (3.12) and (3.13) to get equations of motion for the macroscopic continuum variables ρ, $\mathbf{u}$, and ϵ. The requirement that the continuum equations generated by Eqs. (3.1) and (3.2) match the usual hydrodynamic equations as closely as possible, as well as satisfying the moment relations (2.1)–(2.3), puts constraints on the undetermined coefficients in the equilibrium distribution functions. The constraint relations can be solved to get the following expressions for the coefficients:

$$A_0=\rho-Ab, \tag{3.3}$$

$$A=\frac{D}{bc^2}\left[p_0-\kappa\sum_\gamma \rho\partial_\gamma\partial_\gamma\rho-\kappa\left(\frac{1}{2}-\frac{1}{D'}\right)\sum_\gamma (\partial_\gamma\rho)(\partial_\gamma\rho)\right], \tag{3.4}$$

$$E_{\alpha\beta}=\frac{D(D+2)}{2bc^4}\kappa(\partial_\alpha\rho)(\partial_\beta\rho), \quad \alpha\neq\beta \tag{3.5}$$

$$E_{\alpha\alpha}=\frac{D(D+2)}{2bc^4}\left[\kappa(\partial_\alpha\rho)(\partial_\alpha\rho)-\frac{\kappa}{D'}\sum_\gamma (\partial_\gamma\rho)(\partial_\gamma\rho)\right], \tag{3.6}$$

$$B=\frac{D}{bc^2}\epsilon\left[p_0-\kappa\sum_\gamma \rho\partial_\gamma\partial_\gamma\rho-\kappa\left(\frac{1}{2}-\frac{1}{D'}\right)\sum_\gamma (\partial_\gamma\rho)(\partial_\gamma\rho)\right], \tag{3.7}$$

$$B_0=\rho\epsilon-Bb, \tag{3.8}$$

$$H_{\alpha\beta}=\epsilon E_{\alpha\beta}, \tag{3.9}$$

$$G_\alpha=\frac{D}{bc^2}\left[\Delta t\left(\tau_\epsilon-\frac{1}{2}\right)P_{\alpha\beta}\partial_\beta\epsilon-k\partial_\alpha T\right]. \tag{3.10}$$

The actual physical dimension of the system is denoted by D' and may be smaller than the lattice dimension D on which the simulation is originally developed. For two-dimensional systems, the $E_{\alpha\alpha}$ are explicitly

$$E_{xx}=-E_{yy}=\frac{D(D+2)}{4bc^4}\kappa[(\partial_x\rho)^2-(\partial_y\rho)^2]. \tag{3.11}$$

The variable k appearing in Eq. (3.21) is the thermal conductivity and T is the local temperature.

To second order in Δt, the hydrodynamic equations generated by these equilibrium distributions are

$$\frac{\partial}{\partial t}\rho+\partial_\alpha\rho u_\alpha=0, \tag{3.12}$$

$$\begin{aligned}\frac{\partial}{\partial t}\rho u_\alpha+\partial_\beta\rho u_\alpha u_\beta=&-\partial_\beta P_{\alpha\beta}-\partial_\alpha\zeta\partial_\beta(\rho u_\beta)\\&-\partial_\alpha\xi u_\beta\partial_\beta\epsilon+\partial_\beta\nu\partial_\beta(\rho u_\alpha)\\&+\partial_\beta\nu\partial_\alpha(\rho u_\beta)+\partial_\alpha\nu\partial_\beta(\rho u_\beta),\end{aligned} \tag{3.13}$$

$$\frac{\partial}{\partial t}\rho\epsilon+\partial_\alpha\rho\epsilon u_\alpha=\partial_\alpha k\partial_\alpha T. \tag{3.14}$$

The transport coefficients ζ, ξ, and ν appearing in the momentum equation are given by

$$\zeta=\Delta t\left(\tau_\rho-\frac{1}{2}\right)\frac{\partial p_0}{\partial\rho}, \tag{3.15}$$

$$\xi=\Delta t\left(\tau_\rho-\frac{1}{2}\right)\frac{\partial p_0}{\partial\epsilon}, \tag{3.16}$$

$$\nu=\Delta t\left(\tau_\rho-\frac{1}{2}\right)\frac{c^2}{D+2}. \tag{3.17}$$

The coefficient ν is the kinematic viscosity, but the coefficients ζ and ξ have no counterparts in classical hydrodynamics and must be considered as artifacts of the lattice-Boltzmann method. Similar terms were also found for the single-phase thermal model developed by the authors and by Swift *et al.* in their multiphase isothermal model [6]. For a fixed grid spacing, the time step Δt can be decreased by increasing c. If τ_ρ is simultaneously adjusted so that ν remains fixed, then the coefficients ζ and ξ vanish in the limit of small time step. This occurs because ν is proportional to c^2 while ζ and ξ are not. Numerical comparison of lattice-Boltzmann simulations against known analytic results using the single-phase thermal model suggest that the contribution from these extra dispersion terms is small even for larger values of the time step [7].

Like the original isothermal two-phase model of Swift *et al.*, Eq. (3.13) is not Galilean invariant [6]. For the low-speed flows described here, this should not be a problem [6]. For higher speed flows, Holdych *et al.* have developed a correction that removes the non-Galilean terms from the momentum equation (at least to low order) [17]. Although it has not been done in this paper, the correction can easily be applied to this algorithm and should make it possible to simulate higher speed multiphase flows. The correction scheme may also be used to eliminate the terms proportional to ζ and ξ in Eq. (3.13).

From Eq. (3.10) it is clear that τ_ϵ and k can be treated as independent parameters. This is the approach taken in the simulations described in this paper. The parameter τ_ϵ has no effect on the hydrodynamics, although it may affect the numerical stability of the algorithm. Alternatively, τ_ϵ could be fixed so that the G_α terms only correct the hydrodynamics to eliminate spurious energy flows due to gradients in the density. If the local energy density is considered to be a function of ρ and T then Eq. (3.10) can be rewritten as

$$G_\alpha=\frac{D}{bc^2}\left[\Delta t\left(\tau_\epsilon-\frac{1}{2}\right)P_{\alpha\beta}\left(C_V\partial_\beta T+\frac{\partial\epsilon}{\partial\rho}\partial_\beta\rho\right)-k\partial_\alpha T\right], \tag{3.18}$$

where C_V is the constant volume specific heat. The value of τ_ϵ can be chosen so that the two terms proportional to the gradient of T approximately cancel

$$k=\Delta t\left(\tau_\epsilon-\frac{1}{2}\right)C_V\frac{1}{D'}\mathrm{Tr}\,P_{\alpha\beta}. \tag{3.19}$$

For a single phase, where $P_{\alpha\beta}\sim p_0\delta_{\alpha\beta}$, the temperature terms in G_α cancel exactly and the remaining term is just

proportional to a gradient of the density. This makes sense, since the hydrodynamic equation for the original two-distribution model, in which the thermal energy flux is written as the gradient of the energy, already contains the temperature gradient term. The only correction that is needed is to cancel out the unecessary term proportional to a gradient of the density. For an ideal-gas system, the G_α vanish altogether, as expected. Because ϵ is only a function of T for this case, there is no need for any hydrodynamic corrections.

IV. NUMERICAL IMPLEMENTATION

The numerical implementation of this algorithm is straightforward in most respects. The results described above have been derived assuming that the lattice has suitable isotropy properties [13]. These include the hexagonal lattice in two dimensions and the hypercubic face-centered (HCFC) lattice in four dimensions. The HCFC lattice can be projected down onto the orthogonal lattice in two dimensions ($d2q9$ using Qian's notation [12]) and the $d3q19$ lattice in three dimensions. (The d indicates the dimension of the projected lattice and q signifies the number of independent components in the distribution, including the zero velocity component.) The simulations reported here were all performed on the $d2q9$ two-dimensional lattice. Boundary conditions were implemented using the methods described in a previous paper [7].

The equilibrium distribution functions require the evaluation of both first and second derivatives of the density and first derivatives of the specific energy and temperature. The first and second derivatives of the density are needed to evaluate the coefficients $E_{\alpha\beta}$ and $H_{\alpha\beta}$. The first derivatives are computed using the formula

$$\partial_\alpha \rho = \frac{1}{\Sigma_i w_i} \sum_i w_i \left(\frac{\Delta \rho}{\Delta x_\alpha} \right)_i \tag{4.1}$$

where $(\Delta\rho/\Delta x_\alpha)_i$ is the single-sided finite difference approximation to the first derivative with respect to the coordinate direction x_α. It is calculated from the difference in density at the points $\mathbf{r}$ and $\mathbf{r}+\Delta t\mathbf{e}_i$ and has the form

$$\left(\frac{\Delta \rho}{\Delta x_\alpha} \right)_i = \frac{1}{\Delta t \mathbf{e}_i \cdot \hat{\mathbf{n}}_\alpha} [\rho(\mathbf{r}+\Delta t\mathbf{e}_i) - \rho(\mathbf{r})]. \tag{4.2}$$

The unit vector $\hat{\mathbf{n}}_\alpha$ points along the α coordinate axis. Only the $(\Delta\rho/\Delta x_\alpha)_i$ that can be evaluated and for which $\mathbf{e}_i \cdot \hat{\mathbf{n}}_\alpha$ is nonzero are included in the summation in Eq. (4.1). This form is useful for points located on boundaries where $\rho(\mathbf{r}+\Delta t\mathbf{e}_i)$ may not be defined for all $\mathbf{e}_i$. The weights w_i that appear in Eq. (4.1) reflect the total number of vectors in the original lattice that are projected down into the lower-dimensional lattice. For the $d2q9$ lattice, $w_i=4$ for vectors along the axial directions and $w_i=1$ for vectors along the diagonal directions.

The second derivatives are evaluated using the following finite-difference formula:

$$\frac{\partial f_{0,0}}{\partial x^2} + \frac{\partial f_{0,0}}{\partial y^2} = \frac{1}{6h^2}[f_{1,1}+f_{-1,1}+f_{1,-1}+f_{-1,-1}+4f_{1,0} + 4f_{-1,0}+4f_{0,1}+4f_{0,-1}-20f_{0,0}], \tag{4.3}$$

where h is the lattice spacing and the subscripts on the function f indicate displacements of $\pm h$ in the x or y directions. This equation is obtained by generalizing a standard approximation of the two-dimensional Laplacian to the four-dimensional HCFC lattice and then projecting the result back down to the two-dimensional $d2q9$ lattice. Equation (4.3) cannot be applied directly to boundary points, because not all the $\rho(\mathbf{r}+\Delta t\mathbf{e}_i)$ are defined. For this study, a reflective boundary condition was used to assign densities to neighboring sites that reside in the interior of solid boundaries (for boundary sites at corners or along diagonals, this is done separately for each of the coordinate directions). The second derivative of the density could then be calculated using Eq. (4.3).

The first derivatives of the specific energy and temperature that appear in the definition of the G_α were handled slightly differently. The contribution of the G_α to the equilibrium distribution function F_i^{eq} has the form

$$G_\alpha e_{i\alpha} = \frac{D}{bc^2}\left[\left(\tau_\epsilon - \frac{1}{2}\right)(p\Delta t e_{i\alpha}\partial_\alpha \epsilon + \kappa(\partial_\beta \rho) \times (\partial_\beta \epsilon)\Delta t e_{i\alpha}\partial_\alpha \rho) - \frac{k}{\Delta t}\Delta t e_{i\alpha}\partial_\alpha T\right]. \tag{4.4}$$

Note that the explicit form of the pressure tensor has been substituted into Eq. (3.10) in writing Eq. (4.4). The gradient terms $\Delta t e_{i\alpha}\partial_\alpha \epsilon$, etc. really represent the projection of the gradient of ϵ, ρ, and T onto the displacement vector $\Delta t\mathbf{e}_i$. Instead of using Eq. (4.1) for the first derivatives, these are much better approximated as

$$\Delta t e_{i\alpha}\partial_\alpha \epsilon = \epsilon(\mathbf{r}+\Delta t\mathbf{e}_i) - \epsilon(\mathbf{r}). \tag{4.5}$$

Similar expressions are used for the directional derivatives of ρ and T. The remaining derivatives of ρ and ϵ appearing in Eq. (4.4) are evaluated using Eqs. (4.1) and (4.2). The approximation represented by Eq. (4.5) is essential for describing the behavior of a two-phase system; however, for single-phase compressible flow, the approximation represented by Eq. (4.1) is sufficient.

V. RESULTS

All simulations reported here used the van der Waals equation of state

$$p_0 = \frac{\rho RT}{1-b\rho} - a\rho^2 \tag{5.1}$$

to model the thermodynamic properties of the fluid. The units of temperature are chosen so that the ideal gas constant is $R=1$. The specific energy can be derived in a straightforward way from Eq. (5.1) using the thermodynamic relation [18]

$$\left(\frac{\partial U}{\partial V}\right)_{N,T} = T\left(\frac{\partial p}{\partial T}\right)_{N,V} - p, \tag{5.2}$$

where U is the total internal energy, N is the number of particles, and V is the volume of the system. The result is

$$\epsilon = \frac{3}{2}RT - a\rho. \tag{5.3}$$

Equations (5.1) and (5.3) are all that are needed to completely specify the thermodynamics [Eq. (5.3) can easily be inverted to obtain T as a function of ϵ and ρ]. The critical temperature and density for the van der Waals fluid are $T_c = 8a/(27Rb)$ and $\rho_c = 1/(3b)$ [19]. The parameters a and b for all simulations were chosen to have the values $a = 9/8$ and $b = 1/3$, which sets the critical temperature and pressure at 1. Additional parameters that needed to be set for the simulations were the relaxation parameters τ_ρ and τ_ϵ, the thermal conductivity k, the surface tension parameter κ, and the lattice speed c.

The first simulation using this model was just a simple interface confined between two walls. The simulations were performed on a grid of 103×5 lattice sites, with periodic boundary conditions imposed on the short axis. The simulations were therefore effectively one dimensional. The simulation volume is actually 100 lattice units in length, plus an extra lattice point to include the origin. Two additional lattice sites are required at either end of the simulation volume to implement boundary conditions. Reflective boundary conditions for the mass flux were applied at either end of the system and constant temperature boundary conditions were applied for the specific energy. The reduced temperature at either end of the system was set at $T = 0.8$ and the surface tension parameter in the Cahn-Hilliard equation was chosen to be $\kappa = 0.4$. The spacing on the square grid, Δx, was set to 1.0 and the time step was chosen to be $\Delta t = 0.2$. The particle speed c is completely determined by the choice of Δx and Δt and is equal to $c = \sqrt{2}\Delta x/\Delta t$. The factor of $\sqrt{2}$ comes from the fact that the nearest-neighbor vectors in the original four-dimensional HCFC lattice correspond to vectors running along the diagonals of the two-dimensional $d2q9$ lattice. The relaxation parameters τ_ρ and τ_ϵ were both set equal to 1.0 as was the thermal conductivity k. Enough mass was confined in the system to force it to form a two-phase system with an interface. The simulation was then run until all velocity and thermal transients had damped out. A plot of the resulting density and temperature profile in the vicinity of the interface is shown in Fig. 1. The most important feature of the temperature profile is that it is absolutely flat through the interface, even though the temperature is allowed to vary freely and is not imposed on the system externally. Other simulations, in which the interface was oriented at 45° to the grid axes, showed some deviations from a constant temperature in the vicinity of the interface but these appear to be small (the magnitude of the deviation was sensitive to the value of κ used in the simulation, but was less than 1% in the worst case). Although the dynamics of this system are not very interesting, it is a rigorous test of the model. Several early versions of this algorithm were unable to simulate a simple two-phase fluid profile.

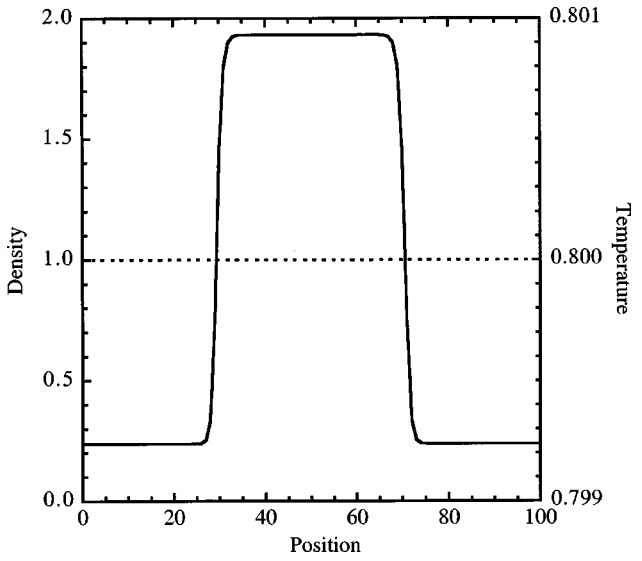

FIG. 1. Temperature and density profiles for a free-standing liquid film at $T = 0.8$. The solid line is density; the dotted line is temperature.

Another test of the algorithm is to check whether or not the normal component of the pressure tensor is constant through the interface. This is a mechanical condition required by a system at equilibrium. The normal and tangential components of the pressure tensor are displayed in Fig. 2. It can be seen that the normal component of the pressure tensor is constant through the interface while the tangential component shows a large deviation from uniformity. This deviation gives rise to the surface tension.

To check that the model correctly reproduces the equilibrium thermodynamics of the system, a series of simulations of the liquid-vapor interface at different temperatures were performed and used to reconstruct the liquid-vapor phase diagram. The results of these simulations, along with the exact result based on the equation of state, are shown in Fig. 3. The agreement between the simulations and the analytic result is nearly perfect.

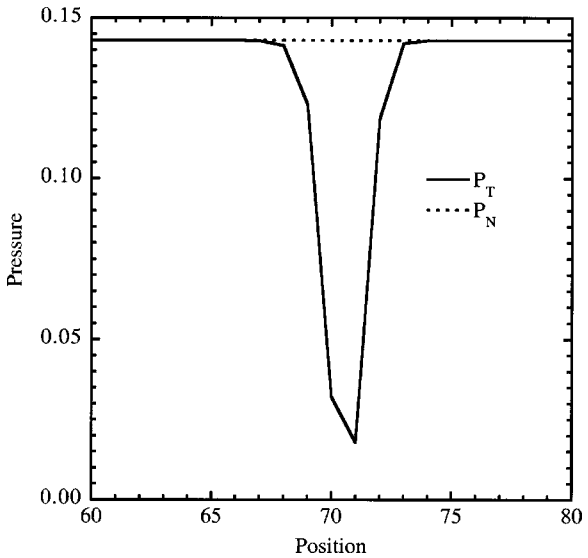

FIG. 2. Normal and tangential components of the pressure tensor for a free-standing liquid film at $T = 0.8$. The solid line is the tangential component; the dotted line is the normal component.

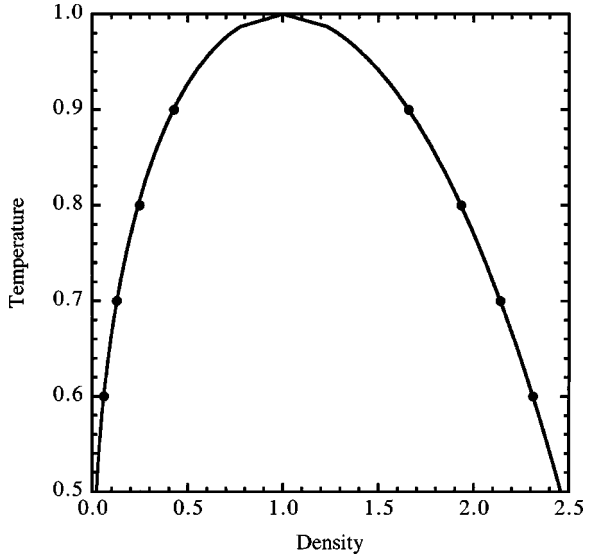

FIG. 3. Comparison of liquid-vapor phase diagram calculated from simulations of a free-standing film (dots) and the analytic result (solid line).

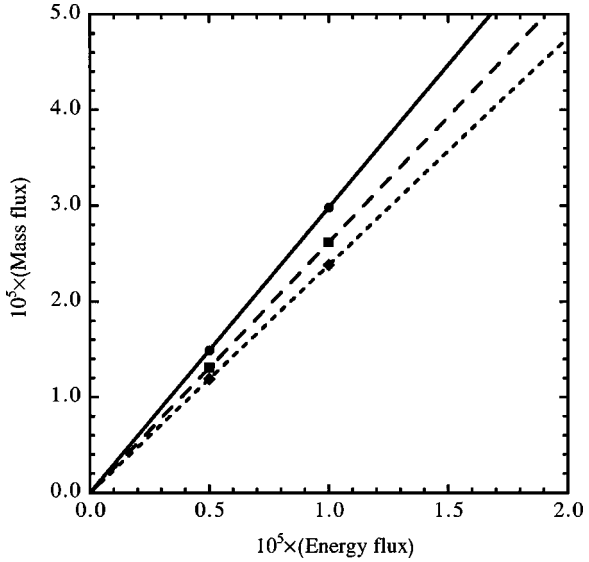

FIG. 4. Comparison of simulated and predicted mass fluxes as a function of energy flux for evaporation of a liquid film on a heated plate. The lines are the predicted fluxes, the symbols are the simulated fluxes. Three different temperatures at the vapor side boundary are shown. (Circle) $T=0.85$. (Square) $T=0.80$. (Diamond) $T=0.75$.

Simulations of a thin liquid film evaporating from a heated plate were used to verify that the the ratio of the heat flux into a liquid-vapor interface over the mass flux out of the interface is equal to the specific enthalpy of vaporization. The specific enthalpy h for the van der Waals equation of state is

$$h=\epsilon\rho-p=\frac{3}{2}RT\rho-\frac{\rho RT}{1-b\rho}. \tag{5.4}$$

The specific enthalpy of vaporization h_{vap} is just $h_{\mathrm{vap}}=h_g-h_l$, where h_g and h_l are the specific enthalpies of the gas and liquid phases. The simulations to test the relation between the fluxes and enthalpy of vaporization were done on a 53×5 lattice. Periodic boundary conditions were again used in the short dimension so that the simulation is effectively one dimensional. The time step was increased slightly to $\Delta t=0.25$, but all other parameters were the same as in the previous example. A constant heat flux boundary condition was imposed at one end of the simulation cell for the energy and a reflective boundary condition was used for the mass. Constant temperature and constant pressure boundary conditions were specified at the other end of the simulation cell and the initial distribution of mass was chosen so that about half the simulation cell was liquid and half the cell was vapor. The liquid half of the cell corresponded to the side with the constant heat flux boundary condition and the vapor side corresponded to the constant temperature boundary condition. The initial temperature throughout the system was set equal to the same temperature used in the constant temperature boundary condition and the liquid and vapor densities were chosen to be equal to the liquid and vapor densities at the coexistence point of the van der Waals liquid at the initial temperature. The pressure specified in the constant pressure boundary condition was set equal to the vapor pressure of the van der Waals liquid at the coexistence point. Under these conditions, the liquid film evaporates steadily after the decay of some initial transients. The mass flux out of the system at the end corresponding to the constant temperature-constant pressure boundary can be calculated. A plot of mass flux vs heat flux should be a straight line with a slope that is equal to the specific enthalpy. A plot of heat flux vs mass flux for several temperatures is shown in Fig. 4. The straight lines included in the figure are the predicted mass fluxes based on the enthalpy of vaporization at the specified temperature. The plot shows almost perfect agreement between the predicted and measured mass fluxes.

Simulations of an evaporating drop were performed using a 203×203 size lattice. A circular boundary of radius 100 was inscribed inside the original square grid and was used to specify both the temperature and pressure for the simulation. The circular boundary was used to minimize the effect of the discrete lattice on the evaporation of the drop. The time step for this simulation was set at $\Delta t=0.2$ and the thermal conductivity was increased to $k=2.0$. A liquid drop of radius 40 was equilibrated with its vapor inside the circular boundary at a temperature of 0.8. The density at the boundary was initially set equal to $\rho_g=0.239$, which is the equilibrium vapor density at $T=0.8$. The system was then equilibrated for 500 steps, after which the density at the boundary was slowly lowered over the next 500 steps to a value of $\rho_g=0.200$. The temperature at the boundary remained at a value of 0.8 throughout the simulation. These boundary conditions resulted in the slow evaporation of the droplet over time.

The behavior of the temperature profile at different times is shown in Fig. 5. The initial response is a rapid cooling in the vicinity of the interface as evaporation draws energy out of the drop. The temperature inside the drop then continues to cool as energy flows out of the interface due to additional evaporation at the drop surface. The initial lowering of the constant density boundary condition appears to result in some strong transients in the simulation; possibly a pressure wave that travels through the drop. These transients cause

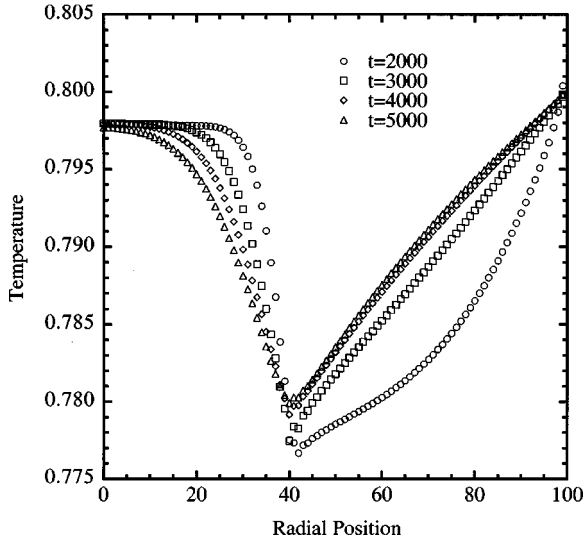

FIG. 5. Temperature profiles for evaporating drop at different times.

the temperature inside the drop to change quickly and uniformly from a value of 0.8 to a slightly lower value of 0.798. The value of the temperature at the interface also appears to rise slightly as the drop evaporates. This may be caused by a slight increase in the vapor density in the vicinity of the drop as the evaporation proceeds. Figure 6 shows some profiles of the density at different times. As expected, the location of the interface moves inward as material from the drop evaporates.

Contour plots of the fluid density and the temperature profile at the end of the simulation are shown in Fig. 7. The plots show that the temperature reaches a minimum at the drop surface and then gradually increases as one moves either into the interior of the drop or towards the circular boundary. Some small nonunformities in the temperature contours are evident in the region near the drop surface. These appear to be due to small, spurious velocities that show up near the interface if the interface is not oriented along the axis directions. Similar spurious velocities were

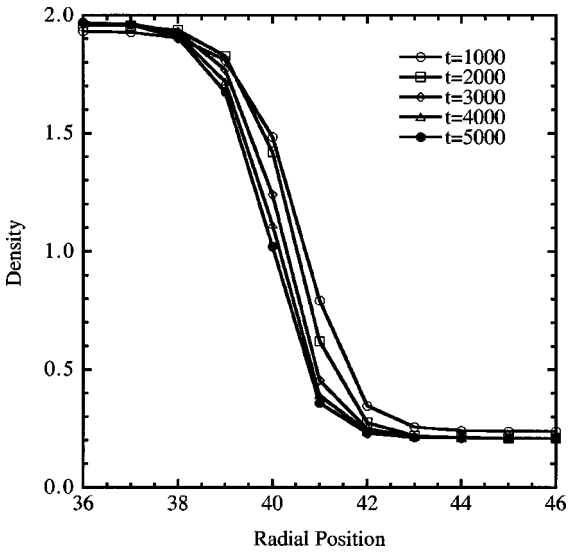

FIG. 6. Density profiles for evaporating drop at different times.

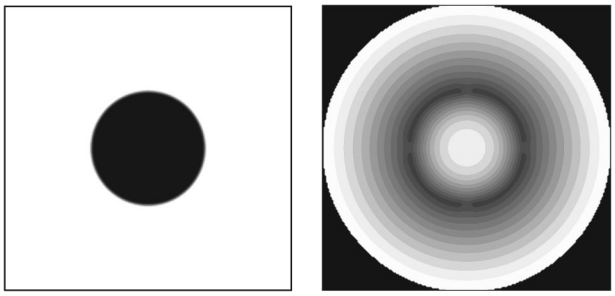

FIG. 7. Gray-scale contour plots of density and temperature for an evaporating drop. Dark regions signify high values for density and low values for temperature. (Left) density. (Right) temperature.

noted by Swift *et al.* [6] in their original isothermal two-phase model.

Finally, results are presented for simulations of condensation in a channel under the influence of gravity. Gravity can be introduced into the simulation by modifying the distribution f_i using the formula

$$f_i' = f_i + \frac{\overline{\rho} D}{bc^2} \mathbf{e}_i \cdot \mathbf{g}, \tag{5.5}$$

where $\overline{\rho}$ is equal to $[\rho(\mathbf{r}) + \rho(\mathbf{r}+\mathbf{e}_i)]/2$ and $\mathbf{g}$ is the gravity vector [7]. The lattice for these simulations was 100×400 lattice units in size with gravity oriented along the long axis of the channel. The top of the channel was maintained at a constant vapor density of 0.236, zero flux boundary conditions were imposed along the sides and bottom of the channel. The temperature boundary conditions were somewhat more complicated. The top of the channel was maintained at a fixed temperature of $T=0.8$. The first 20 lattice sites from the top of the channel along the sides, 1–20, were also held at a temperature of $T=0.8$. The next ten lattice sites, 21–30, were linearly ramped down from $T=0.8$ to $T=0.75$. The remaining lattice sites on the sides and bottom of the channel were held at a temperature of 0.75. Under these conditions, gas flows in from the top of the channel and condenses on the sides. The initial condition consisted of a coating of liquid along the sides of the channel approximately 15 units thick, starting at the beginning of the cool portion of the channel and extending to the bottom. The top of the film at the transition point between hot and cold surfaces was initially rounded to prevent large transients due to surface tension effects. The bottom central portion of the channel was initially free of liquid. The magnitude of $\mathbf{g}$ was set to 0.0001 and the remaining parameters were the same as for the evaporating drop simulation.

Figure 8 shows contour maps of the density and temperature distributions after 20 000 and 60 000 steps. After 20 000 steps, the liquid has started to sag down towards the bottom and is beginning to close off the dry gap that was originally present at the bottom of the channel. After 60 000 steps, the dry gap has been pinched off and the bottom of the channel is completely coated with liquid. The temperature profiles inside the channels are also shown. The temperature profiles vary smoothly across the interface and it is difficult to spot exactly where the interface is, based solely on examining the temperature behavior. The vapor at the bottom of the channel

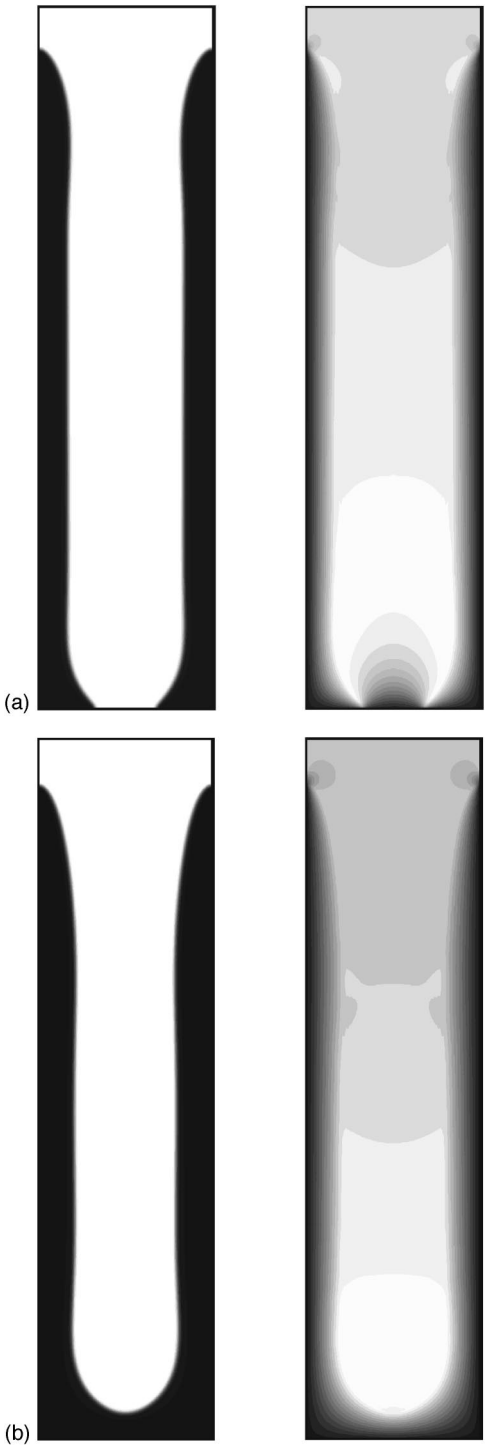

FIG. 8. Gray-scale contour plots of density and temperature for vapor condensing in a channel. Dark regions signify high values for density and low values for temperature. (Top) density (left) and temperature (right) after 20 000 steps. (Bottom) density (left) and temperature (right) after 60 000 steps.

shows a cold spot at shorter times due to the fact that it is in direct contact with the cold surface at the bottom. The temperature plot at longer time, however, indicates that the vapor has heated up slightly in the bottom of the channel and is warmer than the vapor coming in at the top. This is due to the fact that for these conditions, the vapor density is quite large and the effect of gravity on the vapor phase density is significant. The density of the vapor increases noticeably as one moves down the channel, from 0.236 at the top to 0.272 near the bottom. To remain in equilibrium with the higher vapor phase densities, the temperature at the liquid-gas interface must increase near the bottom of the channel. This results in a general warming of the vapor phase. The energy for heating up the vapor comes both from mechanical compression of the gas as it moves down the channel and the release of energy at the vapor-liquid interface as the gas condenses.

VI. CONCLUSIONS

A lattice Boltzmann algorithm for simulating thermal multiphase flows has been described and the macroscopic hydrodynamic equations generated by the model have been derived. Expressions for the macroscopic viscosity and thermal conductivity in terms of the microscopic parameters of the model are also obtained. The algorithm can handle an arbitrary equation of state and correctly reproduces the form of the heat current, even for a nonideal fluid. The model has been tested on several systems to verify that it can reproduce the expected behavior for thermally driven phase changes.

Simulations of a free-standing film showed that the algorithm can reproduce a constant thermal profile through a vapor-liquid interface. The free-standing film can also be used to calculate the coexistence behavior of the fluid as a function of temperature. This can then be compared to the predictions based on the equation of state. For a van der Waals fluid, complete agreement is found.

Simulations of evaporation of a thin liquid film from a heated plate demonstrated that a thermally limited phase change obeys the correct overall energy and mass balance relations. The total amount of material that can evaporate from a surface is related to the heat flux into the surface and the enthalpy of vaporization. Simulations have verified that the ratio of the heat flux into the interface divided by the mass flux of gas out of the interface is equal to the specific enthalpy of vaporization.

Simulations of an evaporating drop show an initial rapid decrease in the surface temperature of the drop followed by a slower development of the temperature profile both inside and outside the drop. The radius of the drop also decreases as evaporation proceeds. Finally, simulations of condensation inside a channel show significant accumulation of fluid in the channel as well as distortion and movement of the liquid-vapor interface. These simulations demonstrate that the thermal two-phase flow algorithm presented here contains the basic physics for simulating the dynamics of thermally driven phase changes. This includes many important processes such as boiling, distillation, and reactions in multiphase systems.

As it stands, the thermal two-phase model is applicable to systems near the critical point and to systems where surface tension effects are large, such as flow in microchannels and porous media. The interface thickness generally increases with increasing surface tension in the Cahn-Hilliard model, so a larger grid spacing can be used at higher surface tensions. The interface also broadens as the system approaches the critical point. For systems with low surface tension, the interface becomes narrow and the grid spacing must be made small, resulting in extremely large grids. Experience with the model also suggests that problems arise at lower tempera-

tures, where the ratio of the liquid to vapor density becomes extremely high and the interface again represents a rapid change in density over a short distance. Lattice-Boltzmann algorithms have recently been described which do not require a regular grid [20,21] and open up the possibility of using a grid with higher resolution in the region of the interface and low resolution elsewhere. Such a grid would eliminate the excess cells in regions outside the interface that occur if regular grids are used. Grid refinement schemes, such as that proposed by Filippova and Hänel [21], are particularly promising in this regard.

APPENDIX

The purpose of this appendix is to provide some of the details in the derivation of the coefficients represented by Eqs. (3.3)–(3.10). Because the equilibrium distribution functions satisfy Eqs. (2.1)–(2.3), the undetermined parameters appearing in the equilibrium distributions must be related by

$$\rho = Ab + A_0 + E_{\alpha\alpha}\frac{bc^2}{D}, \tag{A1}$$

$$\rho\epsilon = Bb + B_0 + H_{\alpha\alpha}\frac{bc^2}{D}. \tag{A2}$$

This can be verified by direct calculation and using the lattice vector relation [13]

$$\sum_{i=1}^{b} e_{i\alpha}e_{i\beta} = \frac{bc^2}{D}\delta_{\alpha\beta}.$$

Use is also made of the property that sums over odd numbered products of lattice vectors vanish. Summing Eq. (3.1) over i and making use of the moment relations gives the following equation for the density:

$$\frac{\partial}{\partial t}\rho + \partial_\alpha \rho u_\alpha = \Delta t\left[\frac{\partial}{\partial t}\left(\tau_\rho - \frac{1}{2}\right)\left(\frac{\partial}{\partial t}\rho + \partial_\alpha \rho u_\alpha\right) + \partial_\alpha\left(\tau_\rho - \frac{1}{2}\right)\left(\frac{\partial}{\partial t}\rho u_\alpha + \partial_\beta \sum_{i=1}^{b} e_{i\alpha}e_{i\beta}f_i^{eq}\right)\right]. \tag{A3}$$

Multiplying Eq. (3.1) by $\mathbf{e}_i$ and then summing over i leads to the momentum equation

$$\frac{\partial}{\partial t}\rho u_\alpha + \partial_\beta \sum_{i=1}^{b} e_{i\alpha}e_{i\beta}f_i^{eq} = \Delta t\left[\frac{\partial}{\partial t}\left(\tau_\rho - \frac{1}{2}\right)\left(\frac{\partial}{\partial t}\rho u_\alpha + \partial_\beta \sum_{i=1}^{b} e_{i\alpha}e_{i\beta}f_i^{eq}\right) + \partial_\beta\left(\tau_\rho - \frac{1}{2}\right)\left(\frac{\partial}{\partial t}\sum_{i=1}^{b} e_{i\alpha}e_{i\beta}f_i^{eq} + \partial_\gamma \sum_{i=1}^{b} e_{i\alpha}e_{i\beta}e_{i\gamma}f_i^{eq}\right)\right]. \tag{A4}$$

Finally, summing Eq. (3.2) over i gives the equation of motion for the energy

$$\frac{\partial}{\partial t}\rho\epsilon + \partial_\alpha \sum_{i=1}^{b} e_{i\alpha}F_i^{eq} = \Delta t\left[\frac{\partial}{\partial t}\left(\tau_\epsilon - \frac{1}{2}\right)\left(\frac{\partial}{\partial t}\rho\epsilon + \partial_\alpha \sum_{i=1}^{b} e_{i\alpha}F_i^{eq}\right) + \partial_\alpha\left(\tau_\epsilon - \frac{1}{2}\right)\left(\frac{\partial}{\partial t}\sum_{i=1}^{b} e_{i\alpha}F_i^{eq} + \partial_\beta \sum_{i=1}^{b} e_{i\alpha}e_{i\beta}F_i^{eq}\right)\right] \tag{A5}$$

From Eqs. (A3)–(A5), it can be seen that to lowest order in Δt, the hydrodynamic equations for this system are

$$\frac{\partial}{\partial t}\rho + \partial_\alpha \rho u_\alpha = 0 + \mathcal{O}(\Delta t), \tag{A6}$$

$$\frac{\partial}{\partial t}\rho u_\alpha + \partial_\beta \sum_{i=1}^{b} e_{i\alpha}e_{i\beta}f_i^{eq} = 0 + \mathcal{O}(\Delta t), \tag{A7}$$

$$\frac{\partial}{\partial t}\rho\epsilon + \partial_\alpha \sum_{i=1}^{b} e_{i\alpha}F_i^{eq} = 0 + \mathcal{O}(\Delta t). \tag{A8}$$

Equations (A6) and (A7) can be used in the mass conservation equation (A3) to eliminate the terms on the right-hand side. This implies that to second order in Δt, the mass conservation equation is given by Eq. (3.12). Similarly, the momentum equation (A4) can be reduced to

$$\frac{\partial}{\partial t}\rho u_\alpha + \partial_\beta \sum_{i=1}^{b} e_{i\alpha}e_{i\beta}f_i^{eq} = \Delta t\,\partial_\beta\left(\tau_\rho - \frac{1}{2}\right)\left(\frac{\partial}{\partial t}\sum_{i=1}^{b} e_{i\alpha}e_{i\beta}f_i^{eq} + \partial_\gamma \sum_{i=1}^{b} e_{i\alpha}e_{i\beta}e_{i\gamma}f_i^{eq}\right) \tag{A9}$$

Using the explicit definition of f_i^{eq} and the lattice vector identity [13]

$$\sum_{i=1}^{b} e_{i\alpha}e_{i\beta}e_{i\gamma}e_{i\delta} = \frac{bc^4}{D(D+2)}(\delta_{\alpha\beta}\delta_{\gamma\delta} + \delta_{\alpha\gamma}\delta_{\beta\delta} + \delta_{\alpha\delta}\delta_{\beta\gamma}),$$

the sums over the f_i^{eq} can be evaluated to get the expressions

$$\sum_{i=1}^{b} e_{i\alpha}e_{i\beta}f_i^{eq} = A\frac{bc^2}{D}\delta_{\alpha\beta} + \rho u_\alpha u_\beta + \frac{bc^4}{D(D+2)}(E_{\gamma\gamma}\delta_{\alpha\beta} + E_{\alpha\beta} + E_{\beta\alpha}), \tag{A10}$$

$$\sum_{i=1}^{b} e_{i\alpha}e_{i\beta}e_{i\gamma}f_i^{eq} = \frac{\rho c^2}{D+2}(\delta_{\alpha\beta}u_\gamma + \delta_{\alpha\gamma}u_\beta + \delta_{\beta\gamma}u_\alpha). \tag{A11}$$

Comparing the momentum equation with Eqs. (A9) and (A10) suggests that the parameters A and the $E_{\alpha\beta}$ can be related to the pressure tensor $P_{\alpha\beta}$ via

$$\left(A\frac{bc^2}{D}+\frac{bc^4}{D(D+2)}E_{\gamma\gamma}\right)\delta_{\alpha\beta}+\frac{bc^4}{D(D+2)}(E_{\alpha\beta}+E_{\beta\alpha}) =P_{\alpha\beta}. \tag{A12}$$

This equation, in combination with Eq. (A1), can be used to determine A, A_0, and the $E_{\alpha\beta}$.

Equations (A1) and (A12) are not sufficient to uniquely determine the quantities A, A_0, and $E_{\alpha\beta}$, so there is some flexibility in choosing one of these parameters. One possibility is to choose A_0 to have the form given by Eq. (3.3) and to choose $E_{\alpha\beta}=E_{\beta\alpha}$. It follows from (A1) that the $E_{\alpha\beta}$ must satisfy the relation

$$\sum_{\gamma}\frac{bc^2}{D}E_{\gamma\gamma}=0. \tag{A13}$$

To avoid confusion in the remaining derivation of the coefficients A and $E_{\alpha\beta}$, the summations over spatial indices have been included explicitly. From Eq. (A12), the $E_{\alpha\beta}$ for $\alpha\neq\beta$ have the form given by Eq. (3.5). For $\alpha=\beta$, it follows from Eq. (A12) that the $E_{\alpha\alpha}$ must also satisfy the relation

$$A\frac{bc^2}{D}+\frac{2bc^4}{D(D+2)}\left(\frac{1}{2}\sum_{\gamma}E_{\gamma\gamma}+E_{\alpha\alpha}\right) =p_0-\kappa\sum_{\gamma}\rho\partial_\gamma\partial_\gamma\rho-\frac{\kappa}{2}\sum_{\gamma}(\partial_\gamma\rho)(\partial_\gamma\rho) +\kappa(\partial_\alpha\rho)(\partial_\alpha\rho). \tag{A14}$$

Simultaneously solving Eqs. (A13) and (A14) for A and the $E_{\alpha\alpha}$ leads to Eqs. (3.4) and (3.6).

The equilibrium distribution f_i^{eq} is now completely determined and the momentum equation to order Δt becomes

$$\frac{\partial}{\partial t}\rho u_\alpha+\partial_\beta\rho u_\alpha u_\beta =-\partial_\beta P_{\alpha\beta}+\Delta t\partial_\beta\left(\tau_\rho-\frac{1}{2}\right)\left[\frac{\partial}{\partial t}P_{\alpha\beta}+\frac{\partial}{\partial t}\rho u_\alpha u_\beta +\frac{c^2}{D+2}\partial_\gamma\rho(\delta_{\alpha\beta}u_\gamma+\delta_{\alpha\gamma}u_\beta+\delta_{\beta\gamma}u_\alpha)\right]. \tag{A15}$$

The $\partial\rho u_\alpha u_\beta/\partial t$ term is second order in u in the dissipation term. It is assumed to be of higher order and is dropped. The remaining time derivative of $P_{\alpha\beta}$ can eventually be converted into an expression containing only spatial gradients. However, this cannot be done until the analysis of the energy equation is completed.

Using the first-order equation for the energy (A8), Eq. (A5) can be simplified to

$$\frac{\partial}{\partial t}\rho\epsilon+\partial_\alpha\sum_{i=1}^{b}e_{i\alpha}F_i^{eq} =\Delta t\partial_\alpha\left(\tau_\epsilon-\frac{1}{2}\right)\left(\frac{\partial}{\partial t}\sum_{i=1}^{b}e_{i\alpha}F_i^{eq}+\partial_\beta\sum_{i=1}^{b}e_{i\alpha}e_{i\beta}F_i^{eq}\right) \tag{A16}$$

The sums over the distribution functions can be evaluated using the definitions of the F_i^{eq} to get

$$\sum_{i=1}^{b}e_{i\alpha}F_i^{eq}=\rho\epsilon u_\alpha+G_\alpha\frac{bc^2}{D}, \tag{A17}$$

$$\sum_{i=1}^{b}e_{i\alpha}e_{i\beta}F_i^{eq}=B\frac{bc^2}{D}\delta_{\alpha\beta}+H_{\gamma\delta}\frac{bc^4}{D(D+2)}(\delta_{\alpha\beta}\delta_{\gamma\delta}+\delta_{\alpha\gamma}\delta_{\beta\delta} +\delta_{\alpha\delta}\delta_{\beta\gamma})+\rho\epsilon u_\alpha u_\beta. \tag{A18}$$

Anticipating the final results, the parameters G_α are assumed to be of order Δt. After dropping terms of order u^2 in the dissipation terms, the energy equation can then be written as

$$\frac{\partial}{\partial t}\rho\epsilon+\partial_\alpha\rho\epsilon u_\alpha =-\partial_\alpha G_\alpha\frac{bc^2}{D}+\Delta t\partial_\alpha\left(\tau_\epsilon-\frac{1}{2}\right)\left[\frac{\partial}{\partial t}\rho\epsilon u_\alpha+\partial_\alpha\frac{bc^2}{D}B +\frac{bc^4}{D(D+2)}(\partial_\alpha H_{\beta\beta}+\partial_\beta H_{\alpha\beta}+\partial_\alpha H_{\beta\alpha})\right]. \tag{A19}$$

Using the first-order equations, the time derivative in the dissipation term can be rewritten as

$$\frac{\partial}{\partial t}\rho\epsilon u_\alpha=-\epsilon\partial_\beta\rho u_\alpha u_\beta-\epsilon\partial_\beta P_{\alpha\beta}-u_\alpha\partial_\beta\rho\epsilon u_\beta -u_\alpha\partial_\beta G_\beta\frac{bc^2}{D}+\epsilon u_\alpha\partial_\beta\rho u_\beta. \tag{A20}$$

Using Eq. (A20) in Eq. (A19) leads to the energy equation

$$\frac{\partial}{\partial t}\rho\epsilon+\partial_\alpha\rho\epsilon u_\alpha =-\partial_\alpha G_\alpha\frac{bc^2}{D}+\Delta t\partial_\alpha\left(\tau_\epsilon-\frac{1}{2}\right)\left[\partial_\beta\frac{bc^2}{D}B\delta_{\alpha\beta}-\epsilon\partial_\beta P_{\alpha\beta} +\frac{bc^4}{D(D+2)}(\partial_\alpha H_{\beta\beta}+\partial_\beta H_{\alpha\beta}+\partial_\beta H_{\beta\alpha})\right]. \tag{A21}$$

The terms of order u^2 and the terms proportional to G_α in the dissipation terms are of higher order and are dropped. A good choice for B and the $H_{\alpha\beta}$ is to require them to satisfy the relation

$$\left(B\frac{bc^2}{D}+\frac{bc^4}{D(D+2)}H_{\gamma\gamma}\right)\delta_{\alpha\beta}+\frac{bc^4}{D(D+2)}(H_{\alpha\beta}+H_{\beta\alpha}) =\epsilon P_{\alpha\beta}. \tag{A22}$$

The similarity between this equation and Eq. (A12) immediately leads to the expressions given in Eqs. (3.7)–(3.9). The energy equation can now be rewritten as

$$\frac{\partial}{\partial t}\rho\epsilon+\partial_\alpha\rho\epsilon u_\alpha=-\partial_\alpha G_\alpha\frac{bc^2}{D}+\Delta t\partial_\alpha\left(\tau_\epsilon-\frac{1}{2}\right)P_{\alpha\beta}\partial_\beta\epsilon. \tag{A23}$$

The dissipation term should be proportional to the gradient of temperature. This requirement leads directly to Eq. (3.10). The energy equation then reduces to Eq. (3.14), which is the traditional form in the absence of viscous heating.

The results for the energy equation can be used to eliminate the time derivative of the pressure tensor in the momentum equation (A15). To lowest order in Δt, the energy equation is

$$\frac{\partial}{\partial t}\rho\epsilon+\partial_\alpha\rho u_\alpha\epsilon=0+\mathcal{O}(\Delta t). \tag{A24}$$

Because the time derivative of the pressure tensor is already in a dissipation term, the gradients in $P_{\alpha\beta}$ can be considered to be contributing to higher order and are dropped. The pressure tensor reduces to

$$P_{\alpha\beta}\sim p_0\delta_{\alpha\beta}.$$

The time derivative of the pressure can then be written as

$$\frac{\partial}{\partial t}P_{\alpha\beta}=-\frac{\partial p_0}{\partial\rho}\partial_\alpha\rho u_\alpha-\frac{\partial p_0}{\partial\epsilon}u_\alpha\partial_\alpha\epsilon. \tag{A25}$$

This can be combined with Eq. (A15) to give Eq. (3.13).

[1] W. Tsai and D. Yue, Annu. Rev. Fluid Mech. **28**, 249 (1996).
[2] B. Ndiga and S. Zaleski, Eur. J. Mech. B/Fluids **15**, 885 (1996).
[3] J. Brackbill, D. Kothe, and C. Zemach, J. Comput. Phys. **100**, 335 (1992).
[4] X. Shan and H. Chen, Phys. Rev. E **47**, 1815 (1993).
[5] X. Shan and H. Chen, Phys. Rev. E **49**, 2941 (1994).
[6] M. Swift, E. Orlandini, W. Osborn, and J. Yeomans, Phys. Rev. E **54**, 5041 (1996).
[7] B. J. Palmer and D. R. Rector, J. Comput. Phys. (to be published).
[8] F. J. Alexander, S. Chen, and J. D. Sterling, Phys. Rev. E **47**, R2249 (1993).
[9] G. R. McNamara, A. L. Garcia, and B. J. Alder, J. Stat. Phys. **81**, 395 (1995).
[10] X. He, S. Chen, and G. Doolen, J. Comput. Phys. **146**, 282 (1998).
[11] H. Chen, S. Chen, and W. H. Matthaeus, Phys. Rev. A **45**, R5339 (1992).
[12] Y. H. Qian, D. d'Humières, and P. Lallemand, Europhys. Lett. **17**, 479 (1992).
[13] U. Frisch, D. d'Humières, B. Hasslacher, P. Lallemand, Y. Pomeau, and J-P. Rivet, Complex Syst. **1**, 649 (1987).
[14] S. Wolfram, J. Stat. Phys. **45**, 471 (1986).
[15] P. L. Bhatnagar, E. P. Gross, and M. Krook, Phys. Rev. **94**, 511 (1954).
[16] J. Cahn and J. Hilliard, J. Chem. Phys. **28**, 258 (1958).
[17] D. J. Holdych, D. Rovas, J. G. Georgiadis, and R. O. Buckius, Int. J. Mod. Phys. C **9**, 1393 (1998).
[18] K. Denbigh, *The Principles of Chemical Equilibrium* (Cambridge University Press, Cambridge, England, 1981), p. 92.
[19] D. A. McQuarrie, *Statistical Mechanics* (Harper & Row, New York, 1973).
[20] X. He and G. Doolen, J. Comput. Phys. **134**, 306 (1997).
[21] O. Filippova and D. Hänel, J. Comput. Phys. **147**, 219 (1998).